Preparation of AC-TiO2 by One-Step Activation Method and the Degradation Properties of Tetracycline Hydrochloride

[1]Mengdi Xu, [1]Bayrammyrat Ovezmyradov, [2]Huiyuan Chen, [1]Hui Nan, [1]Caihong Xue and [1]Guijun Yang*

[1]Qinghai University, Xining, 810016, China.

[2]Qinghai University of Technology, Xining, 810016, China.

junyygg@126.com*

Summary: A one-step activation technique for preparing activated carbon/titanium dioxide (AC-TiO$_2$) photocatalyst was developed in this study, which achieved the expansion of activated carbon and the crystallization transition of titanium dioxide in one step. The properties of the generated materials were examined utilizing photocatalytic degradation of tetracycline hydrochloride (TC). The optimized sample (10%AC-TiO$_2$) has a photocatalytic efficiency of 99.8% in 60 minutes and a degradation efficiency of more than 90% after 5 cycles. According to the experiment results, the combination of AC with TiO$_2$ at high temperatures can induce a considerable number of oxygen vacancies in TiO$_2$, hence increasing the reaction activation site, resulting in improved photocatalytic performance. A strong C-Ti chemical bond can be formed between AC and TiO$_2$. Simultaneously, using AC as the substrate decreases the aggregation problem induced by the small nano size of TiO$_2$ and increases dispersion uniformity. The unique carbon structure with a amount of pore structure can considerably improve the catalyst's adsorption efficacy. Because of the synergistic effect of adsorption-degradation and the perfect photocatalytic activity of TiO$_2$, the composite photocatalyst has exceptional photocatalytic efficiency, opening new possibilities for TiO$_2$ modification.

Introduction

Antibiotic use in both humans and animals is increasing as a result of the fast-paced development of the pharmaceutical and medical industries [1-2]. Antibiotic pollution, also requires consideration for the ecosystem and the surrounding environment, and the persistence and refractoriness of antibiotics will result in significant environmental issues [3]. One of ten antibiotics allowed for livestock growth, tetracycline hydrochloride (TC), is frequently found in drinking water, sewage, and sediment [4, 5]. The continual growth in TC content in water poses a threat to human life and health because of its refractory biodegradability and stability [6-7]. It has become a major topic in recent years to Fig out how to reduce the environment impact of TC.

Nano-semiconductors have received a lot of attention recently because of their excellent potential for catalytic [8-10]. In recent decades, photocatalytic technology has been one of the most prominent topics due to the conversion and use of solar energy [11]. As a result, photocatalytic technology has enormous potential for tackling antibiotic concerns in aquatic environments. Common semiconductor nanocatalysts used in the photocatalytic remediation of organic pollutants in water include ZnO, TiO$_2$, WO$_3$, ZnS, and g-C$_3$N$_4$ [12-13].

Among various transition metal oxides, TiO$_2$ is widely used as a photocatalyst due to its unique characteristics of low cost, good optical activity, high chemical stability, and non-toxicity [14-15]. However, due to its wide band gap, pure TiO$_2$ can only utilize ultraviolet light, and the high recombination efficiency of electrons and holes leads to its low catalytic efficiency in practical use [16-17]. Sheet-like two-dimensional (2D) materials having unique optical and electrical capabilities, as well as great chemical and thermal stability. At the same time, it has a large specific surface area, which permits its internal charges to migrate quickly and directly to the outer surface under illumination, allowing it to conduct surface interactions with other semiconductor materials more efficiently [18-19]. In addition, optimize structural or chemical modification can effectively address some issues with TiO$_2$ and enhance photocatalytic effectiveness such as by doping elements or importing oxygen vacancies

---

in the TiO_2 lattice to change its internal energy band structure and reduce the energy band gap of light [20]. Metal/nonmetal doping is a well-known approach for reducing catalyst band gaps, improving electron and hole separation efficiency, and increasing photocatalytic activity.

Carbon has the advantages of low prices and simple access to raw materials because it's abundant in nature. It has been noted that carbon, a nonmetal, can shrink the band gap of TiO_2 by generating hybrid orbitals, boosting the absorption of visible light [21]. J. Matos. and Wu. J. M. *et al.* employed carbon-doped TiO_2 photocatalyst for enhanced methylene blue degradation under visible light [22, 23]. G.Murali *et al.* created an activated carbon sphere and nanocomposite with TiO_2 nanoparticles to improve photocatalytic water splitting due to improved photon harvesting ability and the construction of a suitable pathway for effective charge separation and migration [24]. Furthermore, activated carbon with a high specific surface area can be employed not only as a doping element source, but also as a matrix material to prevent TiO_2 agglomeration and boost the active site. This method of synthesizing the two materials separately and then combining them is straightforward and quick to adopt, but it can result in weak interfacial interaction between the two phases, causing sample instability after repeated cycles and a loss in catalytic activity.

In reaction on the issues mentioned above, we offer a one-step activation method for producing an AC-TiO_2 photocatalyst and investigate the degrading performance. For the purpose of making activated carbon, we employ agricultural waste hemp straw as the carbon source, and the raw materials are easily accessible and reasonably priced. The expansion of activated carbon and transformation of titanium dioxide crystal form are accomplished simultaneously utilizing a one-step activation process with tetra butyl titanate as the titanium source. Activated carbon and titanium dioxide can form strong C-Ti chemical bonds in a high temperature environment, which increases the catalyst's cycle stability; at the same time, the combination of carbon materials and TiO_2 can cause titanium dioxide to produce a large number of oxygen vacancies during the high temperature process, thereby increasing the reaction activation site, decreasing the catalyst band gap, and improving the photocatalytic efficiency. The carbon structure of the pore structure can also significantly improve the adsorption effect of the catalyst by adsorbing TC during the dark reaction

stage of photocatalysis. The composite photocatalyst has superior good photocatalytic efficiency and offers a novel method for altering titanium dioxide due to the synergistic effect of adsorption-degradation and the unique photocatalytic activity of titanium dioxide.

Experiment

Preparation of experimental samples

Since all the chemicals used in the experiment are analytically pure, no additional processing is necessary. Deionized water is the only type of water required for the experiment. 10 g of hemp straw powder should be well dissolved in 100 mL of 6% KOH, then the mixture should be transferred to a hydrothermal kettle and heated to 190 °C for one hour to promote reaction. To extract the activated carbon precursor PAC, centrifuge Separate, remove the KOH aqueous solution, and dry at 80 °C for 12 hours after cooling to room temperature; Tetrabutyl titanate was used as the titanium source, and 10 ml of the compound was applied dropwise to 150 ml of solution in a water bath set at 80 °C. Titania precursor P-TiO_2 was created using a 0.3mol/L NaOH solution, agitated for 24 hours, transferred to a hydrothermal kettle, and heated to 180°C for 12 hours. Following complete grinding of PAC and P-TiO_2 in accordance with various mass ratios, they were activated in a high temperature tube furnace while being shielded from oxygen to produce AC-TiO_2. The composite photocatalyst AC-TiO_2 was created by drying it at 80 °C for 12 hours after being cleaned with acid and alcohol. As represented by 10%, 20%, 30%, 40%, and 50% AC-TiO_2, the mass ratios of PAC: P-TiO_2 are 1:0.1, 1:0.2, 1:0.3, 1:0.4, and 1:0.5, respectively. The preparation procedures for the control samples of TiO_2 and AC-TiO_2 are identical to those described previously.

Characterization

To ascertain the crystal phase composition of the samples, X-ray difffraction (XD8 Advance A25, Bruke, Germany) with Cu-K radiation was used to detect X-ray diffffraction patterns (XRD). Utilize a field emission scanning electron microscope (FE-SEM) to examine the sample's morphology. N_2 adsorption-desorption isotherm was used to analyze the sample's Brunauer-Emmett-Teller (BET) specific surface area. To examine the alterations of functional groups on the sample's surface, a Fourier infrared spectrometer was employed. A photoelectron spectrometer was used to analyze data from X-ray

photoelectron spectroscopy (XPS). An ultraviolet-visible spectrophotometer (Agilent Technologies Cary 60 UV-Vis) was used to measure the absorbance of the tetracycline hydrochloride solution.

Photocatalytic Performance Test of Composite Materials

Tetracycline hydrochloride (TC) degradation was used to test the produced compounds' photocatalytic activity. In order to mix the photocatalyst uniformly, 100 mg of photocatalyst was typically added to 100 ml of a tetracycline hydrochloride solution at a concentration of 100 mg/L. The solution was agitated in the dark for 30 minutes prior to the light source's illumination to bring the reaction system to adsorption-desorption equilibrium. A 300 W simulated sun light source was utilized to illuminate the liquid after 30 minutes from a location 13 cm distant (bought from Shanghai Hefan Instrument Co., Ltd.). In each photodegradation experiment, a circulating water bath was used to keep the reaction temperature at 25 °C while stirring, and the photodegradation reaction lasted one hour. Every 10 minutes during the reaction, 5 ml of sample was withdrawn from the sample solution, and the solid in the solution was subsequently removed using centrifugal filtration. The degradation rate $(\%)=(C_0-C)/C_0 100\%$ was then computed from the concentration of tetracycline hydrochloride as measured using a UV-Vis spectrophotometer at a wavelength of 358 nm. where C_0 and C are the tetracycline concentrations before and after the reaction, respectively, under visible light irradiation. The findings demonstrate that the composite photocatalyst has the optimum catalytic effect when the mass ratio of PAC: P-TiO$_2$ is (1:0.1), and the degradation efficiency can reach 99.8% after 1 hour of photocatalysis.

Results and Discussion

Structure and morphology

The structural characteristics of different samples were further assessed using XRD. The XRD patterns of AC, TiO$_2$, ground AC-TiO$_2$, and 10% AC-TiO$_2$ are displayed in Fig. 1, and demonstrates that AC is a typical amorphous material. The 2θ=25 °, 38 °, 48 °, 54 °, 55 °, 63 °, and 68 °, which correspond to the (101), (004), (200), (105), (211),

(204), and (116) faces, are where the typical peaks from AC-TiO$_2$ are found [25]. In addition, the sintered TiO$_2$ has a twin crystal structure with a small amount of rutile phase, and its typical characteristic peaks are located at 2θ=28 °(110), 36 °(101), 41 °(111) and 57 °(220) [26]. The presence of anatase and rutile phases causes a homojunction to form in the composites, speeding electron and hole transfer rates and improving photocatalytic activity [27-28].
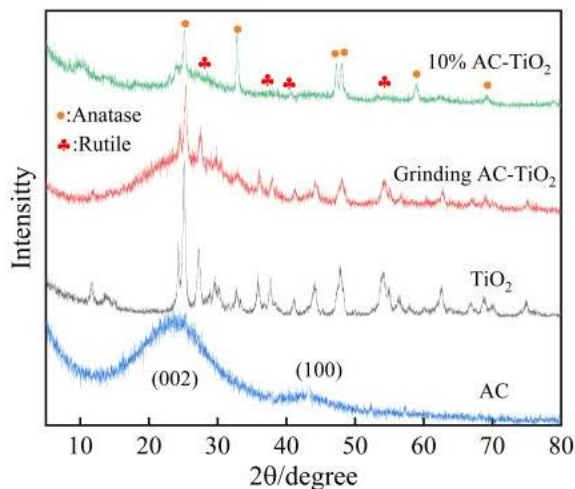

Fig. 1:   XRD spectra of AC, TiO$_2$, Grinding AC-TiO$_2$ and 10% AC-TiO$_2$.

Scanning electron microscopy pictures of 10% AC-TiO$_2$ are displayed in Fig. 2(a)-(b), and the flake TiO$_2$ is more evenly distributed on the surface of the porous activated carbon and has improved dispersibility. This is because spreading TiO$_2$ on the surface of AC improves catalyst dispersion uniformity, recovery efficiency, and cycle stability. The EDS distribution diagrams for (b) are (e) through (g), and they demonstrate TiO$_2$ is evenly spread across the AC surface. Transmission electron microscopy images of 10% AC-TiO$_2$ are shown in (c) through (d). The closely bonded TiO$_2$ nanosheets and AC are shown in Fig. 2(c). Fig. 2(d) analyzes the TiO$_2$ crystal structure, and the (001) and (101) crystal planes of the anatase have interplanar spacings of 0.47 nm and 0.35 nm, respectively [29-31]. This agrees with the XRD test results, and the homojunction form is the primary factor in the photocatalyst's successful catalysis.
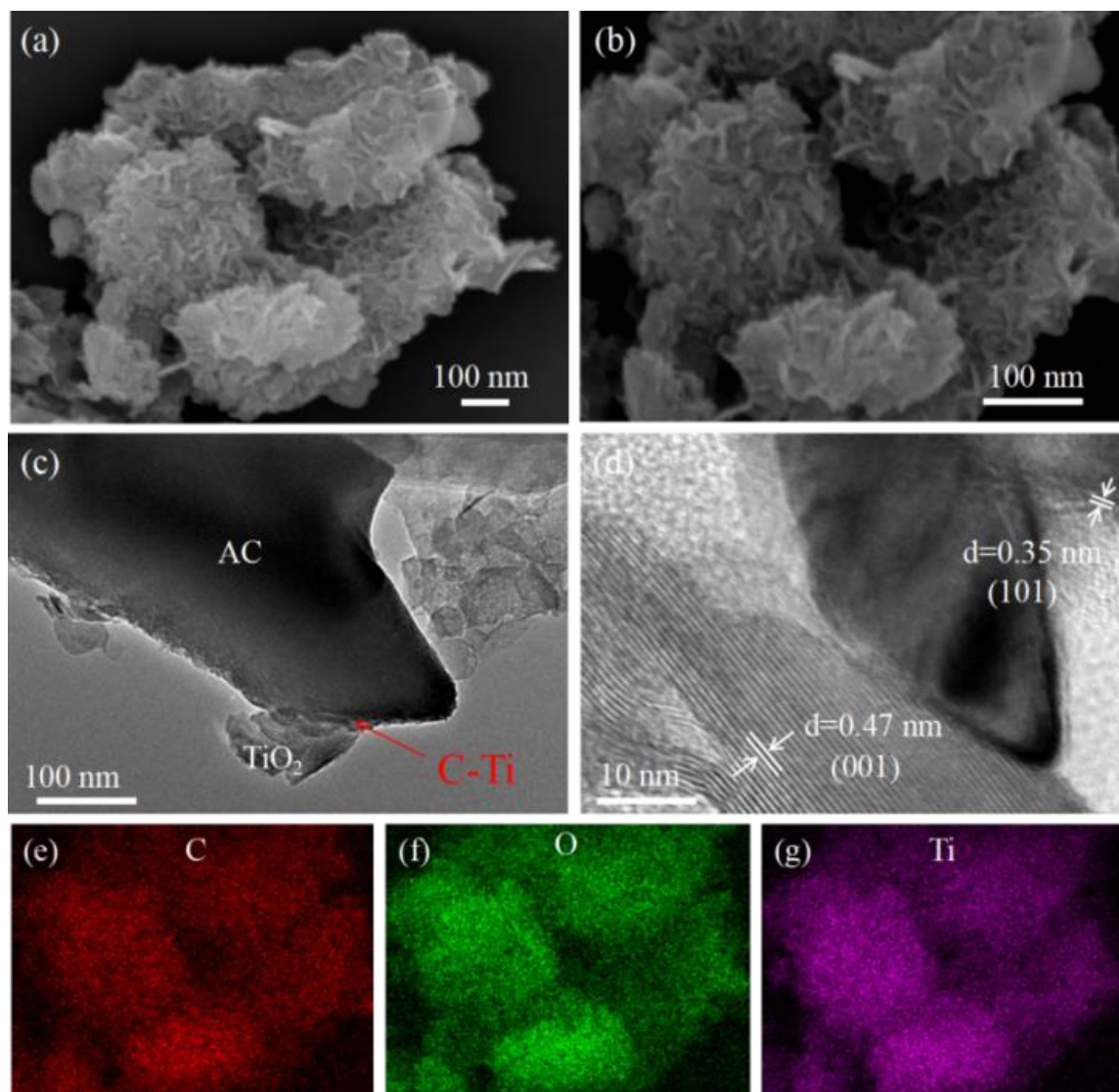
Fig. 2:   (a), (b) The SEM images, (c), (d) The TEM images and (e), (f), (g) EDS images of 10% AC-TiO$_2$.

The surface chemical composition and states of ground AC-TiO$_2$ and 10% AC-TiO$_2$ nanocomposite were examined using XPS measurements. The high-resolution O 1s and Ti 2p spectra from XPS are shown in Fig. 3(a) and (b), respectively. Two peaks at 529.9 eV and 531.5 eV, corresponding to lattice oxygen in Ti-O bonds and oxygen chemisorbed at oxygen vacancies, respectively, are present in the O 1s spectra of Fig. 3(a) [32, 33] . The peak O$_V$ intensity dramatically increased for 10% AC-TiO$_2$, indicating an increase in oxygen vacancies. This is crucial for boosting the photocatalytic activity and increasing the active sites

on the material's surface. Two parallel peaks at 458.9 eV (Ti 2p3/2) and 464.6 eV (Ti 2p1/2) in Fig 2(b) demonstrate the presence of TiO$_2$ in the composite [34, 35]. Notably, another peak around 460.8 eV for 10% AC-TiO$_2$ can be assigned to the strong chemical bonding Ti-C bond [36-38]. This bond is essential to loading TiO$_2$ onto the surface of the AC, demonstrating that for 10% AC-TiO$_2$, TiO$_2$ binds to AC mostly by chemical bonds and some C element doped on the TiO$_2$ phases. It is consistent with the experiment's predictions and the primary cause of the composite material's significant catalytic impact.
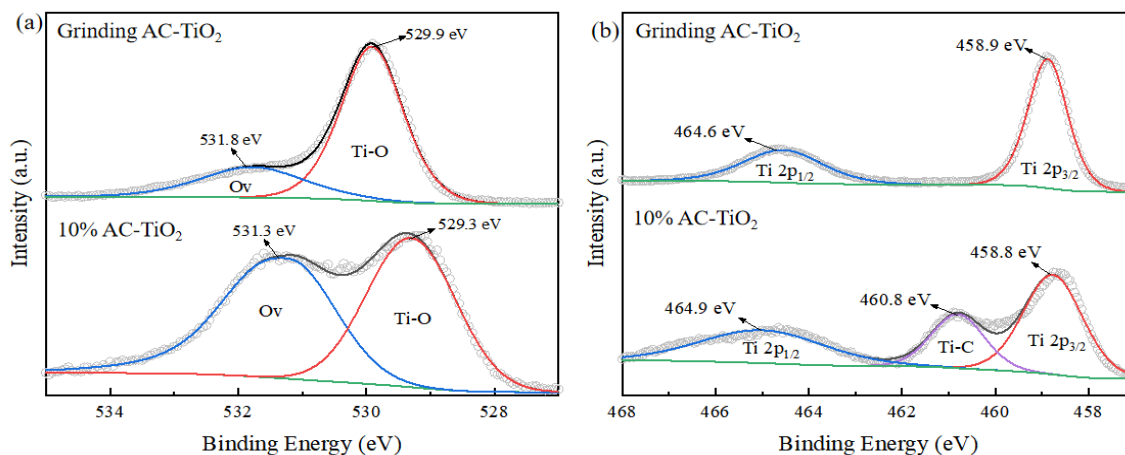
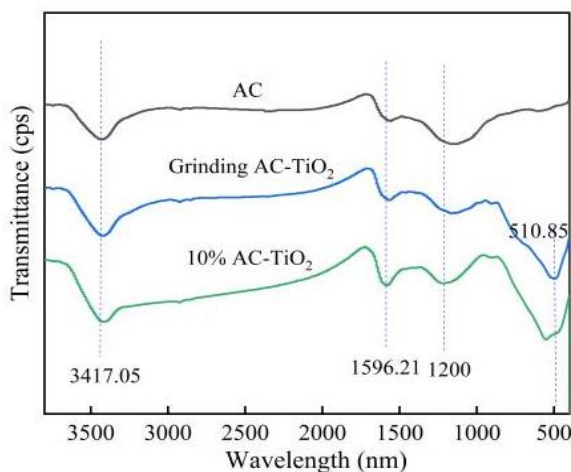Fig. 3:   (a), (b) XPS spectra of Grinding AC-TiO2 and 10% AC-TiO$_2$.

Fig. 4:   FT-IR spectra of AC, Grinding AC-TiO$_2$ and 10% AC-TiO$_2$.

Fig. 4 displays the FT-IR spectra of AC, ground AC-TiO$_2$, and 10% AC-TiO$_2$. The stretching vibration peaks of the sample's adsorbed water -OH are located between 3600 cm^{-1} and 1600 cm^{-1} in the spectra of all three materials [39]. The latter's presence may have In order to speed up the photocatalytic reaction, it is advantageous to produce hydroxyl radicals (OH) in contact with the catalyst surface during the photocatalytic stage. The stretching vibration peak of the C-O bond is located close to its peak position of 1200 cm^{-1}; for grinding AC-TiO$_2$ and 10% AC-TiO$_2$, the same broad mountains at 500-700 cm^{-1} are Ti-O bonds [4, 39] demonstrating the successful synthesis of TiO$_2$. The specific surface areas and pore structure characteristics of the three photocatalysts were

characterized via N$_2$ adsorption-desorption method and the results were shown in Fig. 5. As can be seen, the three photocatalysts belong to the mesoporous materials, but the specific surface area of the 10% AC-TiO$_2$ is 800 m$^2 \cdot$g^{-1} greater than that of TiO$_2$ alone. The pore diameter distribution is shown in Fig. 5 (b). The maximum pore diameter distribution of 10% AC-TiO$_2$ and ground AC-TiO$_2$ is essentially the same, measuring around 3 nm, which is significantly less than the diameter distribution of TiO$_2$. The great adsorption capacity of the catalyst in the dark reaction stage is due to its wide specific surface area, plentiful pore structure, and uniform pore size, which also creates favorable conditions for the quick transfer of TC to the active site.

The Raman spectra of AC, ground AC-TiO$_2$, and 10% AC-TiO$_2$ in the ranges of 0-1000 cm^{-1} and 1000-2000 cm^{-1}, respectively, are shown in Fig. 6(a) and (b). The distinct peaks of 10% AC-TiO$_2$ can be seen in Fig. 6(a) at 155, 198, 393, 513, and 635 cm^{-1}, which are the Raman characteristic peaks of TiO$_2$. This is because during the calcination process, the oxygen inside the distorted TiO$_2$ crystal will diffuse to the outside to produce oxygen vacancies, resulting in the broadening of the spectral peaks [40]. The typical Raman peaks for the disordered sp3 (D band) and conjugated sp2 (G band) of carbon atoms in Fig. 3(b) are situated at 1345 cm^{-1} and 1600 cm^{-1}, respectively. I$_d$/I$_g$ ratios are 0.960, 1.012, and 1.041, respectively—not much of a difference. It is clear that loading of metal oxides has little impact on AC flaws, and as a result, the loading of metal oxides plays a major role in improving the photocatalytic efficiency of composites.
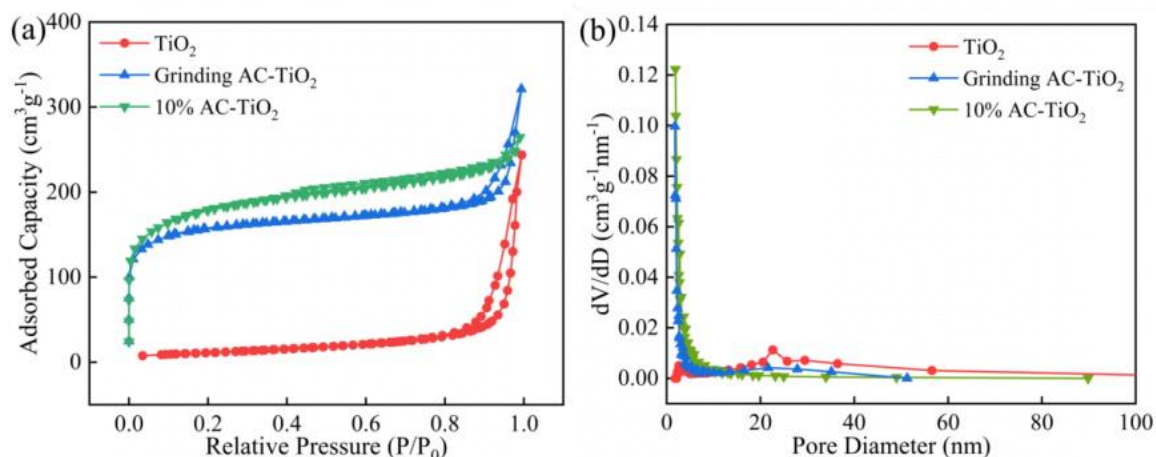
Fig. 5:   (a) Nitrogen adsorption - desorption isotherm and (b) Pore size distribution of TiO_2, Grinding AC-TiO_2 and 10% AC-TiO_2.
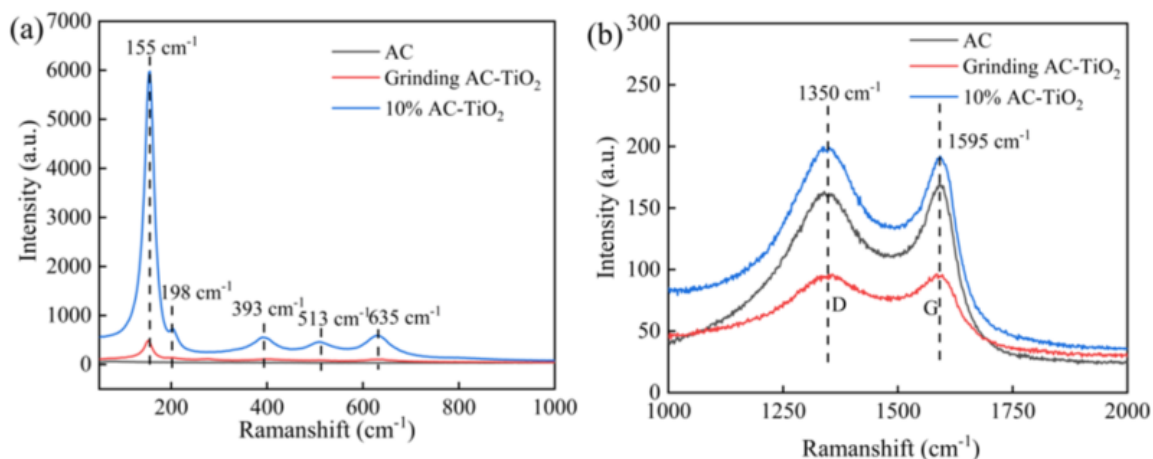

Fig. 6:   (a), (b) The Raman spectroscopy of AC, Grinding AC-TiO_2, and 10% AC-TiO_2.

Photocatalytic performance

The photocatalyst's light responses are governed by its light absorptivity. Fig. 7 shows the TC degradation performance of the catalyst under the irradiation of simulated sunlight, and a first-order kinetic formula is used to fit $\ln(C_0/C)=kt$ [21], where C_0 and C are the concentrations of pollutants in the solution at time 0, respectively, and t and k are the photocatalysis rate constants. This is done using kinetic fitting using kinetic data from relevant literature. The photocatalyst made by the activation approach is better to other photocatalysts in all aspects of adsorption performance and photocatalytic performance, and the catalytic efficiency can reach 60 min after photodegradation 99.8%. Fig. 7(a)

compares TiO_2, ground AC-TiO_2, and 10% AC-TiO_2. This is as a result of the following factors. First, during the high-temperature activation process, numerous oxygen vacancies are created, which helps to increase the photocatalytic efficiency. Secondly, during the activation process, titanium dioxide produces two crystal structures of the anatase and rutile phases, forming a homogenous junction. Thirdly, the lamellar TiO_2 can provide more reactive sites, improving photocatalytic efficiency; and finally, using AC as a carrier increases TiO_2 dispersion uniformity. It is advantageous to the separation of electrons and holes and improves photocatalytic efficiency. The presence of AC also enhances the catalyst's ability to adsorb substances, leading to the formation of a high concentration of tetracycline

hydrochloride inside the catalyst that aids in the process of degradation. Because of this, the 10% AC-TiO$_2$ photocatalyst has very high photocatalytic efficiency.

In order to ascertain whether photocatalysis is a significant factor in the degradation process, there is a adsorption desorption experiment to prove that TC is degraded. As shown in Fig. 7 (c), the dark reaction was continued after the adsorption equilibrium was reached, and then the TC was desorbed. The absorbance of the solution was measured, and the ratio of C/C$_0$ was determined. C/C$_0$ was significantly larger, indicating that TC was only adsorbed and not decomposed. Under the same conditions, the desorption experiment after the light reaction showed no significant change in C/C$_0$, and it was determined that TC was adsorbed to the surface of the catalyst first, and TC was degraded after illumination. Furthermore, the cycle stability test of 10% AC-TiO$_2$ indicates that the degrading efficiency of the catalyst within 60 minutes is still greater than

90% after five cycles, showing that the photocatalyst has strong cycle stability and that the C-Ti bond is stable. The crucial significance of enhancing photocatalyst cycle stability reflects the fundamental role of photocatalytic effects in the catalytic reaction on the side.

Principles of Photocatalysis

The XRD examination on the photocatalyst after five cycles (denoted as 10% AC-TiO$_2$-C) to evaluate the damage caused by the catalytic process, as shown in Fig. 8. The Fig. 8 shows that the catalyst is a twofold crystal structure of anatase and rutile phases. 2θ=25 °, 48 °, 54 °, 55 °, 63 °, 68 °, corresponding to (101), (200), (105), (211), (204), (116) of TiO$_2$ anatase phase, respectively crstal face. The rutile phase's typical characteristic peaks are located at 2=28 ° (110), 36 ° (101), 41 °(111), and 57 °(220). This is the same as the crystal structure before cycling, and show the stability of catalyst.
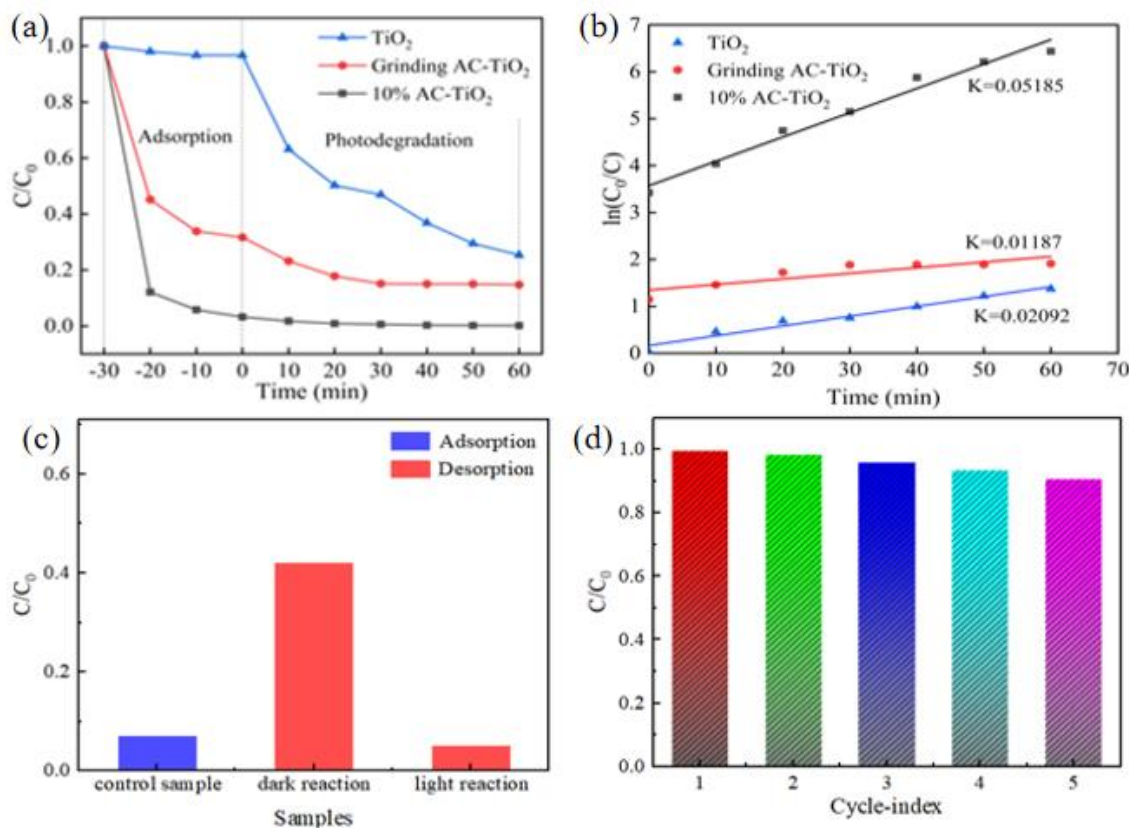

Fig. 7:   (a), (b) Photocatalytic degradation of TC solution and Pseudo-first-order kinetic plots by AC, Grinding AC-TiO$_2$, and 10% AC-TiO$_2$, (c) desorption experiment and (e) cycle stability of 10% AC-TiO$_2$.
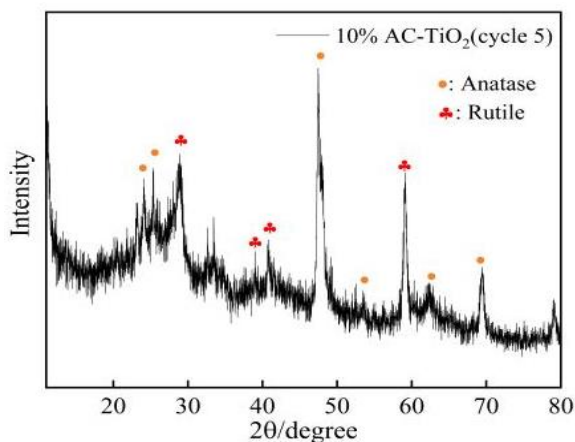
Fig. 8:   XRD patterns of 10% AC-TiO$_2$ after five cycles.

The UV diffuse reflectance spectrum of the material is shown in Fig. 9(a). It can be seen from a comparison of the spectra of the four samples that TiO$_2$ has an excitation wavelength of about 420 nm. The catalyst is changed into full-wavelength absorption with the addition of AC. This has major implications for increasing visible light absorption by photocatalysts and increasing photocatalytic efficiency. The forbidden bandwidths of contrast TiO$_2$, ground AC-TiO$_2$, and 10% AC-TiO$_2$ are, respectively, 3.43 eV, 3.20 eV, and 2.42 eV, as can be shown from Fig. 9(b) on the relationship between (ahv)1/2 and photon energy, it is obvious that 10% AC-TiO$_2$ has the narrowest band gap. According to the empirical formula: E$_{CB}$ = E$_{VB}$ − E$_g$, further, explore the photocatalytic mechanism of composite materials. The conduction band, valence band, and band gap of the photocatalyst are denoted by the letters E$_{CB}$, E$_{VB}$, and E$_g$, respectively [41, 42]. For 10% AC-TiO$_2$, E$_{VB}$ can be obtained through the XPS valence band spectrum (Fig. 9 (c)), which is 2.01 eV, and E$_g$ is 2.42 eV according to DRS analysis (Fig. 9 (b)). Therefore, E$_{CB}$ = E$_{VB}$ − E$_g$ =2.01 − 2.42 = -0.41 eV.

The material's PL picture is shown in Fig. 9(d). We may observe that the materials' fluorescence characteristics gradually deteriorate. The electron-hole pair recombination efficiency of the substance increases with fluorescence, but photocatalytic activity decreases with increasing fluorescence. So 10% AC-TiO$_2$ has the best photocatalytic effect [43].
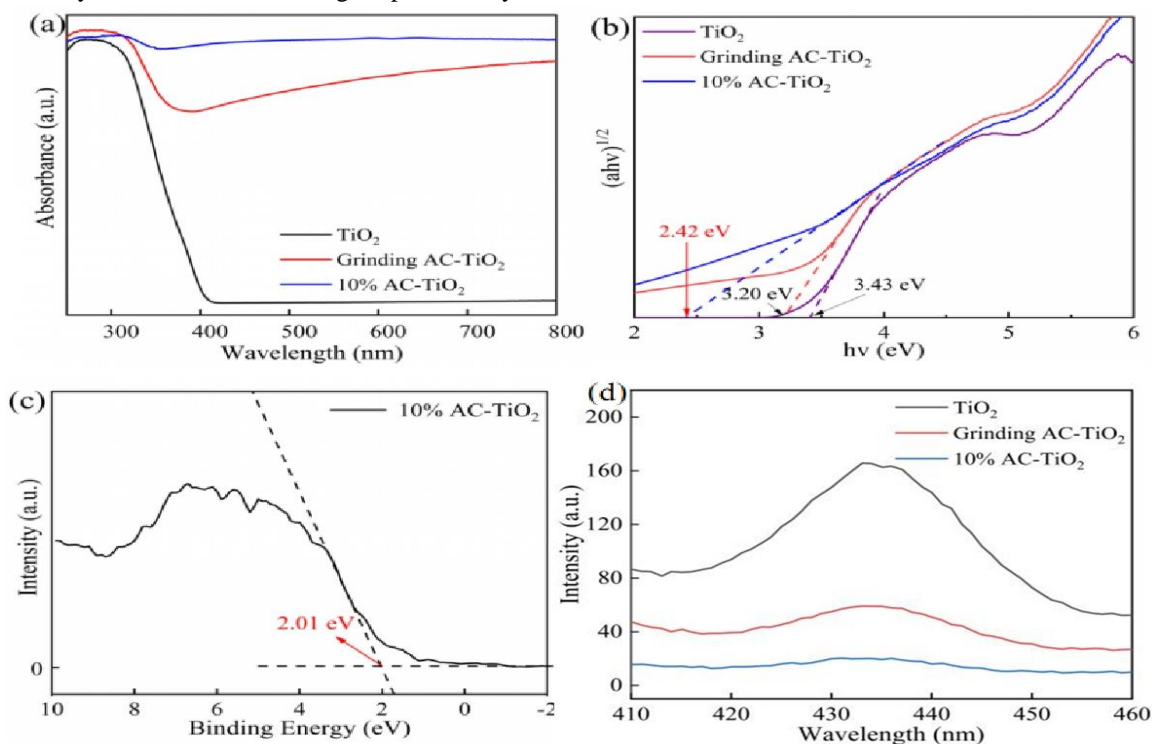

Fig. 9:   (a), (b) The DRS spectroscopy of AC, Grinding AC-TiO$_2$, and 10% AC-TiO$_2$, (c) Valence band XPS spectra of the AC/TiO$_2$, (d) Fluorescence spectra of TiO$_2$, Grinding AC-TiO$_2$ and 10% AC-TiO$_2$.
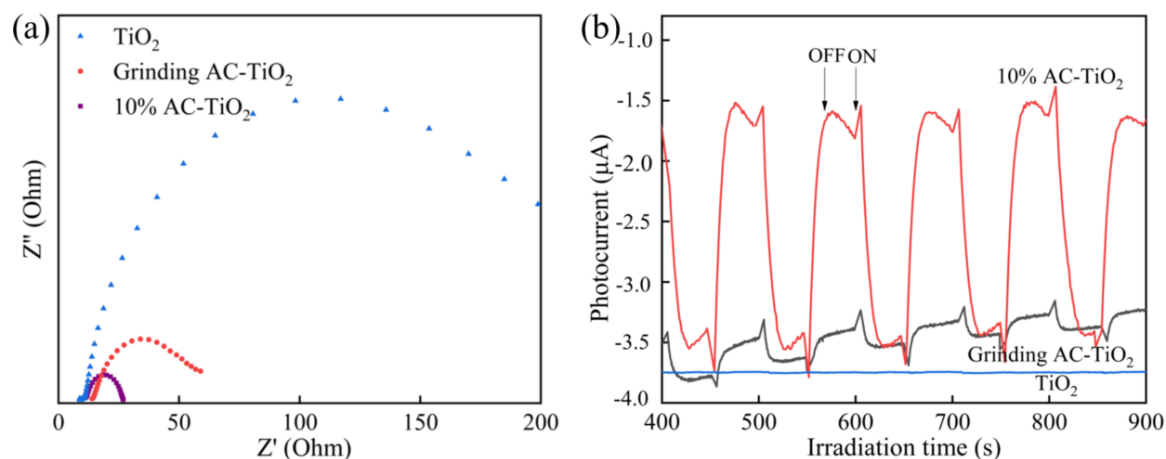
Fig. 10:　(a) Electrochemical impedance spectroscopy and (b) transient photocurrent response of the as-prepared TiO_2, Grinding AC-TiO_2, and 10% AC-TiO_2 materials.

The electrochemical impedances (EIS) of AC, TiO_2, ground AC-TiO_2, and 10% AC-TiO_2 were investigated to demonstrate the effect of heterojunctions with a large number of charge transfer channels on photoexcited separation and carrier transfer efficiency [44]. Fig. 10(a) shows that with 10% AC-TiO_2, the radius of the semicircular arc drops dramatically. The impedance value decreases as the semicircle radius decreases. This shows that the photogenerated carriers of the 10% AC-TiO_2 photocatalytic composite minimize their charge transport barrier. As a result, the composite material exhibits outstanding photochemical characteristics, speeding the transfer of photogenerated electron holes and having a high photocatalytic degradation efficiency. The transient photocurrent can effectively reflect the creation, separation, and movement of photogenerated carriers. Fig. 10(b) shows that the transient currents of TiO_2, ground AC-TiO_2, and 10% AC-TiO_2 are weakened sequentially, indicating that the separation of electrons and holes is sequentially enhanced, proving that the catalysis of 10% AC-TiO_2 is the strongest, which is consistent with the previous analysis results.

Fig. 11 depicts an EPR investigation of Grinding AC-TiO_2 and 10% AC-TiO_2. The g value of

both is equal to 2.003, demonstrating that TiO_2 produces a certain amount of oxygen vacancies during the high-temperature activation process, but the peak height of 10% AC-TiO_2 is much higher than that of Grinding AC-TiO_2, demonstrating that the one-step activation of AC and TiO_2 can effectively promote the generation of oxygen vacancies, which is consistent with the XPS analysis. The many oxygen vacancies can give more reactive sites for the photocatalytic reaction, increasing photocatalytic efficiency [45, 46].
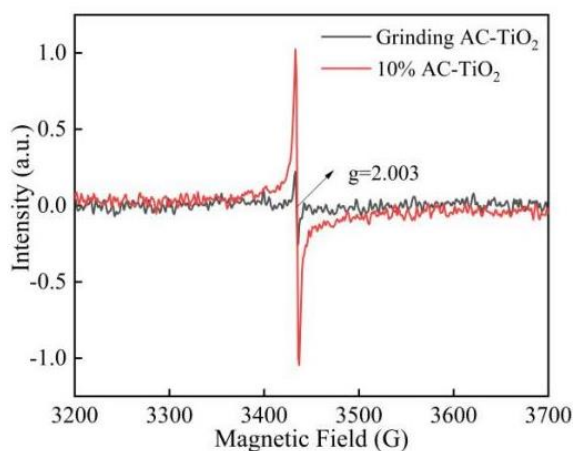

Fig. 11: The EPR spectra of Grinding AC-TiO_2, and 10% AC-TiO_2.

The redox potentials of ·OH/OH$^-$ and O$_2$/O$_2$·$^-$ are +1.99 eV and −0.282 eV [47, 48], respectively. As a result, during the photocatalytic process, TiO$_2$ absorbs sunlight to generate electrons and holes, O$_2$ absorbs electrons and reduces to O$_2$, and H$_2$O oxidizes with holes to produce OH. In conclusion, Fig. 12 depicts the photocatalytic reaction mechanism. Under the synergistic effect of adsorption and catalysis, the AC-TiO$_2$ photoatalyst generated by the one-step activation technique demonstrates good photocatalytic performance. During the dark reaction stage, the porous activated carbon adsorbs a substantial amount of TC, generating a high concentration of degraded chemicals inside the catalyst. At the same time, during the high-temperature activation process of activated carbon doped TiO$_2$, not only is the crystal transformation of TiO$_2$ realized, but the formation of a homojunction improves the separation efficiency of electrons and holes, but also many oxygen vacancies are generated at the same time, increasing the reactive sites; finally, the one-step high-temperature AC-TiO$_2$ alteration in the future opens new avenues for research.

Conclusion

The one-step activation approach used in this study to prepare AC-TiO2 for sintering increased the photocatalyst's catalytic effectiveness and cycling stability. A new study proposal for the combination of activated carbon and titanium dioxide is presented via the one-step sintering method, which can unite AC and TiO2 through the C-Ti chemical link, considerably enhancing the photocatalytic activity and cycle stability. The activation of activated carbon and the transformation of titanium dioxide from an amorphous structure to an anatase crystal form and rutile phase are accomplished during the heating activation process. This results in the formation of a homojunction, which speeds up the transfer rate of electrons and holes and increases the photocatalytic activity. The oxygen inside the deformed TiO2 crystal diffuses to the outside during the calcination process, generating oxygen vacancies, introducing oxygen vacancies, and increasing the reaction activation sites. AC with a high specific surface area and flaky TiO2 have a synergistic adsorption-degradation action, which boosts catalytic efficiency. The catalytic efficiency reached 99.8% in 60 minutes and remained above 90% after five recycling.
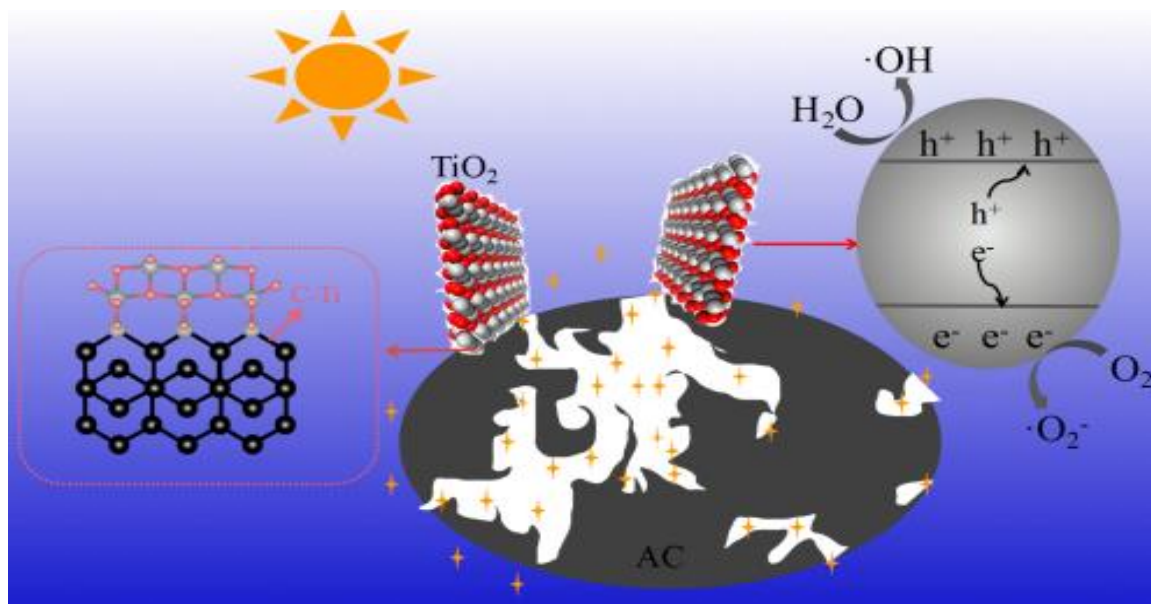

Fig. 12:　Mechanism of the photocatalytic degradation of TC by 10% AC-TiO$_2$ under simulated sun light source irradiation.

Conflict of Interest

The authors declare no conflict of interest.

References

1. Z. Wei, J. Liu, W. Shangguan, A review on photocatalysis in antibiotic wastewater: Pollutant degradation and hydrogen production, *Chinese J. Catal.,* **41**, 1440 (2020).

2. C. Hou, H. Liu, M.F. Bakhtari, Preparation of Ag SPR-promoted TiO_2-{001}/$HTiOF_3$ photocatalyst with oxygen vacancies for highly efficient degradation of tetracycline hydrochloride, *Mater Sci Semicond Process.,* **136**, 106142 (2021).

3. V. K. Sharma, N. Johnson, L. Cizmas, T. J. McDonald, H. Kim, A review of the influence of treatment strategies on antibiotic resistant bacteria and antibiotic resistance genes, *Chemosphere*, **150**, 702 (2016).

4. Z. Huang, J. Wang, M. Q. Yang, Q. Qian, X. P. Liu, L. Xiao, H. Xue, Construction of TiO_2-Eggshell for Efficient Degradation of Tetracycline Hydrochloride: Sunlight Induced In-Situ Formation of Carbonate Radical, *Materials*, **14**, 1598 (2021).

5. Y. Wang, L. Qiu, S. Bao, F. Tian, J. Sheng, W. Yang, Y. Yu. Visible-light enhanced peroxymonosulfate activation on Co_3O_4/MnO_2 for the degradation of tetracycline: Cooperation of radical and non-radical mechanisms, *Sep. Purif,* **316**, 123779 (2023).

6. N. Le-Minh, S. J. Khan, J. E. Drewes, R. M. Stuetz, Fate of antibiotics during municipal water recycling treatment processes, *Water Res*, **44**, 4295 (2010).

7. Y. Yang, W. Song, H. Lin, W. Wang, L. Du, W. Xing, Antibiotics and antibiotic resistance genes in global lakes: A review and meta-analysis, *Environ Int*, **116**, 60 (2018).

8. L Li, F Tian, L Qiu, F Wu, W Yang, Y Yu, Recent Progress on Ruthenium-Based Electrocatalysts towards the Hydrogen Evolution Reaction, *catalysts,* **13**, 1497 (2023).

9. Y. Wang, L. Qiu, S. Bao, F. Tian, L. He, W. Yang, Y. Liu, Y. Yu, In situ construction of $MnIn_2S_4$/$Ti_3C_2T_x$ MXene Schottky junction composites for efficient photoreduction and recovery of U(VI), *Chem. Eng. J*, **468**, 143768 (2023).

10. Y. Wang, S. Bao, X. Liu, L. Qiu, J. Sheng, W. Yang, Y. Yu, Regulating the peroxymonosulfate activation on N doped δ-MnO_2 nanoshttes for tetracycline degradation: N species as the degradation pathways switcher to convert radical to nonradical, *Chem. Eng. J.* **477**, 147050 (2023).

11. X. Ruan, X. Cui, Y. Cui, X. Fan, Z. Li, T. Xie, K. Ba, G. Jia, H. Zhang, L. Zhang, W. Zhang, X. Zhao, J. Leng, S. Jin, D.J. Singh, W. Zheng, Favorable Energy Band Alignment of TiO_2 Anatase/Rutile Heterophase Homojunctions Yields Photocatalytic Hydrogen Evolution with Quantum Efficiency Exceeding 45.6%, *Adv. Energy Mater.,* **12**, 2200298 (2022).

12. M. Gao, F. Tian, X. Zhang, Z. Chen, W. Yang, Y. Yu, Improved Plasmonic Hot-Electron Capture in Au Nanoparticle/Polymeric Carbon Nitride by Pt Single Atoms for Broad-Spectrum Photocatalytic H2 Evolution, *Nanomicro Lett,* **15**, 129 (2023).

13. S. Feizpoor, A. Habibi-Yangjeh, K. Yubuta, Integration of carbon dots and polyaniline with TiO_2 nanoparticles: Substantially enhanced photocatalytic activity to removal various pollutants under visible light, *J. Photochem.,* **367**, 94 (2018).

14. A. Shoja, A. Habibi-Yangjeh, M. Mousavi, S. Vadivel, Preparation of novel ternary TiO_2 QDs/CDs/AgI nanocomposites with superior visible-light induced photocatalytic activity, *J. Photochem.,* **385**, 112070 (2019).

15. N. Madkhali, C. Prasad, K. Malkappa, H. Y. Choi, V. Govinda, I. Bahadur, R. A. Abumousa, Recent update on photocatalytic degradation of pollutants in waste water using TiO_2-based heterostructured materials, *Results in Engineering*, **17**, 100920 (2023).

16. T. Fotiou, T. M. Triantis, T. Kaloudis, K. E. O'Shea, D. D. Dionysiou, A. Hiskia, Assessment of the roles of reactive oxygen species in the UV and visible light photocatalytic degradation of cyanotoxins and water taste and odor compounds using C-TiO_2, *Water Res*, **90**, 52-61 (2016).

17. R. Basumatary, B. Basumatary, D. Konwar, A. Ramchiary, Tailored highly efficient Co-doped TiO_2/$CoTiO_3$ heterojunction photocatalyst for

methylene blue degradation under visible light, *J. Korean Ceram.,* **60,** 547 (2023).

18. X. Zhang, F. Tian, X. Lan, Y. Liu, W. Yang, J. Zhang, Y. Yu, Building P-doped MoS₂/g-C₃N₄ layered heterojunction with a dual-internal electric field for efficient photocatalytic sterilization, *Chem. Eng. J.,* **429,** 132588 (2022).

19. R. Yang, Y. Fan, Y. Zhang, L. Mei, R. Zhu, J. Qin, J. Hu, Z. Chen, Y. Hau Ng, D. Voiry, S. Li, Q. Lu, Q. Wang, J.C. Yu, Z. Zeng, 2D Transition Metal Dichalcogenides for Photocatalysis, *Angew. Chem. Int. Ed.,* **62,** e202218016 (2023).

20. M. Esmat, H. El-Hosainy, R. Tahawy, W. Jevasuwan, N. Tsunoji, N. Fukata, Y. Ide, Nitrogen doping-mediated oxygen vacancies enhancing co-catalyst-free solar photocatalytic H₂ production activity in anatase TiO₂ nanosheet assembly, *Appl. Catal. B.,* **285,** 119755(2021).

21. T. T. T. Le, T. D. Tran, Photocatalytic Degradation of Rhodamine B by C and N Codoped TiO₂ Nanoparticles under Visible-Light Irradiation, *J Chem-Ny.,* 4310513 (2020).

22. J.-M. Wu, Q.-E. Zhao, Activation of carbon cloth and concurrent precipitation of titania nanowires for enhanced adsorption and photocatalysis performance, *Appl. Surf. Sci,* **527,** 146779(2020).

23. J. Matos, A. García, L. Zhao, M.M. Titirici, Solvothermal carbon-doped TiO₂ photocatalyst for the enhanced methylene blue degradation under visible light, *Appl Catal A-Gen.,* **390,** 175 (2010).

24. G. Murali, S. Gopalakrishnan, S. K. Lakhera, B. Neppolian, S. Ponnusamy, S. Harish, M. Navaneethan, Enhanced solar light-driven hydrogen evolution of activated carbon sphere supported TiO₂ hybrid nanocomposites, *Diam Relat Mater.,* **128,** 109226(2022).

25. S. j. Li, Y. Y. Li, L. X. Shao, C. D. Wang, Direct Z-scheme N-doped TiO₂/MoS₂ Heterojunction Photocatalyst for Photodegradation of Methylene Blue under Simulated Sunlight, *ChemistrySelect,* **6,** 181(2021).

26. C. Peng, T. Zhou, P. Wei, H. Ai, B. Zhou, H. Pan, W. Xu, J. Jia, K. Zhang, H. Wang, H. Yu, Regulation of the rutile/anatase TiO₂ phase junction in-situ grown on –OH terminated Ti₃C₂T (MXene) towards remarkably enhanced photocatalytic hydrogen evolution, *Chem. Eng. J.,* **439,** 135685 (2022).

27. Chengwei Qiu, Jinjin Lin,Jinni Shen, *et al.* Regulation of the rutile/anatase TiO2 heterophase interface by Ni12P5 to improve photocatalytic hydrogen evolution[J], Catal. Sci. Technol., **10,** 3709-3719 (2020)

28. Yannan Liu, Xuhui Zou, Lifen Li, Zhangfeng Shen, *et al.* Engineering of anatase/rutile TiO2 heterophase junction via in-situ phase transformation for enhanced photocatalytic hydrogen evolution[J], *J. Colloid Interface Sci,* **599,**795 (2021).

29. Y. Li, K. Lv, W. Ho, F. Dong, X. Wu, Y. Xia, Hybridization of rutile TiO₂ (rTiO₂) with g-C₃N₄ quantum dots (CN QDs): An efficient visible-light-driven Z-scheme hybridized photocatalyst, *Appl. Catal. B.,* **202,** 611 (2017).

30. T. Lertvanithphol, P. Limnonthakul, C. Hom-on, P. Jaroenapibal, C. Chananonnawathorn, S. Limwichean, P. Eiamchai, V. Patthanasettakul, K. Tantiwanichapan, A. Sathukarn, N. Nuntawong, A. Klamchuen, H. Nakajima, P. Songsiriritthigul, M. Horprathum, Facile fabrication and optical characterization of nanoflake aluminum oxide film with high broadband and omnidirectional transmittance enhancement, *Opt. Mater.,* **111,** 110567 (2021).

31. Y. Zhong, R. Wang, J. Chen, C. Duan, Z. Huang, S. Yu, H. Guo, Y. Zhou, Surface-Terminated Hydroxyl Groups for Deciphering the Facet-Dependent Photocatalysis of Anatase TiO₂, *ACS Appl. Mater. Interfaces.,* **14,** 17601 (2022).

32. V. Natu, M. Benchakar, C. Canaff, A. Habrioux, S. Célérier, M.W. Barsoum, A critical analysis of the X-ray photoelectron spectra of Ti₃C₂T_z MXenes, *Matter,* **4,** 1224 (2021).

33. K. Wu, L. Zhou, C. Mao, Y. Chu, Solvothermal synthesis of ZnO with controllable morphology, *Mater. Lett.,* **341,** 134161 (2023).

34. Z. Zheng, J. Wang, P. Bi, J. Ren, Y. Wang, Y. Yang, X. Liu, S. Zhang, J. Hou, Tandem Organic Solar Cell with 20.2% Efficiency, *Joule,* **6,** 171 (2022).

35. L. Gao, D. Lu, Y. Yang, R. Guan, D. Zhang, C. Sun, S. Liu, X. Bian, Amorphous TiO₂₋ₓ modified Sb nanowires as a high-performance sodium-ion battery anode, *J Non Cryst Solids,* **581,** 121396 (2022).

36. X. He, M. Wu, Z. Ao, B. Lai, Y. Zhou, T. An, S. Wang, Metal-organic frameworks derived C/TiO₂ for visible light photocatalysis: Simple synthesis and contribution of carbon species, *J Hazard Mater.,* **403,** 124048 (2021).

37. Y. Gong, R. Tu, T. Goto, High-speed deposition of titanium carbide coatings by laser-assisted metal–organic CVD, *Mater. Res. Bull.,* **48,** 2766 (2013).

38. S. Kumar, D. Kang, H. Hong, M.A. Rehman, Y.J. Lee, N. Lee, Y. Seo, Effect of $Ti_3C_2T_x$ MXenes etched at elevated temperatures using concentrated acid on binder-free supercapacitors, *RSC Adv,* **10**, 41837 (2020).

39. C. Xu, F. Yang, B. Deng, Y. Zhuang, D. Li, B. Liu, W. Yang, Y. Li, Ti_3C_2/TiO_2 nanowires with excellent photocatalytic performance for selective oxidation of aromatic alcohols to aldehydes, *J Catal.,* **383**, 1 (2020).

40. V. Kumaravel, S. Rhatigan, S. Mathew, M.C. Michel, J. Bartlett, M. Nolan, S.J. Hinder, A. Gascó, C. Ruiz-Palomar, D. Hermosilla, S.C. Pillai, Mo doped TiO_2: impact on oxygen vacancies, anatase phase stability and photocatalytic activity, *J. Phys. Condens. Matter.,* **3**, 025008 (2020).

41. X. Li, B. Kang, F. Dong, Z. Zhang, X. Luo, L. Han, J. Huang, Z. Feng, Z. Chen, J. Xu, B. Peng, Z.L. Wang, Enhanced photocatalytic degradation and H2/H2O2 production performance of S-pCN/$WO_{2.72}$ S-scheme heterojunction with appropriate surface oxygen vacancies, *Nano Energy.,* **81**, 105671 (2021).

42. X. Zou, Y. Dong, J. Ke, H. Ge, D. Chen, H. Sun, Y. Cui, Cobalt monoxide/tungsten trioxide p-n heterojunction boosting charge separation for efficient visible-light-driven gaseous toluene degradation, *Chem. Eng. J.,* **400**, 125919 (2020).

43. X. Zheng, H. Han, J. Liu, Y. Yang, L. Pan, S. Zhang, S. Meng, S. Chen, Sulfur Vacancy-Mediated Electron–Hole Separation at MoS_2/CdS Heterojunctions for Boosting Photocatalytic N_2 Reduction, *ACS Appl. Energy Mater.,* **5**, 4475 (2022).

44. X. Guo, L. Qiu, M. Li, F. Tian, X. Ren, S. Jie, S. Geng, G. Han, Y. Huang, Y. Song, W. Yang, Y. Yu, Accelerating the generation of NiOOH by in-situ surface phosphating nickel sulfide for promoting the proton-coupled electron transfer kinetics of urea electrolysis, *Chem. Eng. J*, **483**, 149264 (2024).

45. [45] S. Liu, L. Lu, C. Zhu, Q. Fang, S. Song, Y. Zheng, Y. Shen, The Role of Dual Vacancies in TiO_2 for Enhanced Photocatalytic Hydrogen Generation and Pollutants Removal, *ChemCatChem.,* **14**, e202201107 (2022).

46. X. Kang, G. Dong, T. Dong, Oxygen Vacancy Defect Engineering of Heterophase Junction TiO_2: Interfacial/Surface Oxygen Vacancies Coadjust the Photocatalytic ROS Production, *ACS Appl. Energy Mater.,* **6**, 1025 (2022).

47. E. C. Ogoko, H. I. Kelle, O. Akintola, N. O. Eddy, Experimental and theoretical investigation of Crassostrea gigas (gigas) shells based CaO nanoparticles as a photocatalyst for the degradation of bromocresol green dye (BCGD) in an aqueous solution, *Biomass Convers. Biorefin.,* **23**, 03742 (2023).

48. Y. Li, D. D. Cheng, Y. Luo, L. X. Yang, Coaxial Fe_2O_3/TiO_2 nanotubes for enhanced photo-Fenton degradation of electron-deficient organic contaminant, *Rare Metals,* **40**, 3543 (2021).